

Validation of commercial Bi₂Te₃-based thermoelectric generator modules for application as metrological reference samples

Pawel Ziolkowski^{*}, Przemyslaw Blaschkewitz^a, Eckhard Müller^{a,b}

^aGerman Aerospace Center (DLR) – Institute of Materials Research, Linder Höhe, D-51147 Cologne, Germany

^bInstitute of Inorganic and Analytical Chemistry, Justus Liebig University Gießen, Heinrich-Buff-Ring 17, D-35392 Gießen, Germany

* Corresponding Author: Pawel Ziolkowski; Email: pawel.ziolkowski@dlr.de

ABSTRACT

Traceability and the definition of uncertainty budgets are considered as necessary prerequisites for a meaningful characterization of thermoelectric generator modules (TEM). Due to the lag of standardized measurement techniques and characterization guidelines users and developers of measurement facilities cannot express uncertainty budgets on a normative base, but can only rely on own experiences and act according to best practise approaches. Reference samples are an appropriate method to investigate the accuracy of measurements and to provide insights into strengths and weaknesses of the employed characterization methods. Such references are still not available to date for measurements on TEM. In order to overcome this deficit this article discusses the applicability of commercially available Bi₂Te₃-based TEM to serve as metrological reference samples.

Four TEM types from different manufacturers were investigated with regard to their stability, which was assessed on the base of the internal electric resistance R_i in the course of different experiments. The modules have been tested under constant temperature differences ($\Delta T = 150^\circ\text{C} / 175^\circ\text{C}$) but variable mechanical pressure ($2 \text{ MPa} \leq p \leq 3.5 \text{ MPa}$). Further experiments have been conducted under constant pressure ($p = 3 \text{ MPa}$) and variable temperature differences in order to determine the short-term stability. The long-term stability was assessed from thermal cycling experiments with observation times between 117 h and 443 h in dependence of the observed module stability. Significant differences could be observed regarding the stability of R_i , which ranged from very stable module types with maximum changes of $\Delta R_i < 2.5\%$ to modules with a relatively weak stability showing $\Delta R_i > 13\%$. The sample-to-sample variation (homogeneity) of R_i was tested in a last step on five modules from two most stable types.

Keywords: Thermoelectric Generator Module, Reference Sample, Standardization, Stability, Pressure Sensitivity, Uncertainty Budget, Resistivity

1. INTRODUCTION

Application of thermoelectric generator (TEG) systems is considered to improve the efficiency of industrial processes [1,2,3] and mobile applications [4,5,6,7] by direct conversion of waste heat into electric energy. TEG comprise one or several thermoelectric generator modules (TEM) and typically application specific configurations of heat exchanging components in order to absorb and reject heat from or to heat reservoirs, respectively. Each TEM contains a variable number of p/n thermocouples,

which are connected electrically in series by metallic bridges (Figure 1) and operate under a temperature difference between a heat source and a heat sink. In response to this temperature difference a thermovoltage is generated due to the Seebeck effect [8]. The thermovoltage can be tapped at the terminals of the module in order to supply electric consumers.

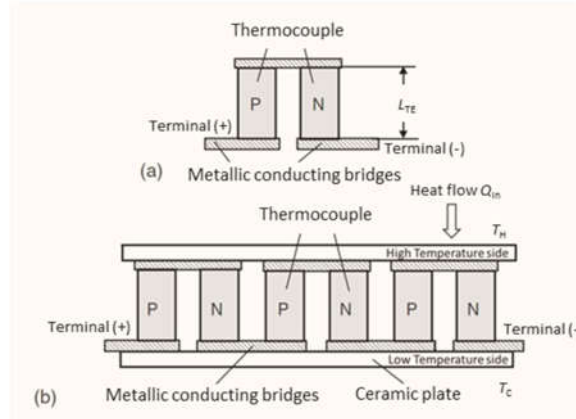


Figure 1: Schematic of a thermocouple (a) as the basic element for a TEM (b). The incident heat flow Q_{in} is absorbed at the hot side of the TEM, which operates at T_H , and released at the cold temperature side, which is kept at T_C . A thermovoltage, which can be tapped at its terminals, is generated by the TEM due to the Seebeck effect.

The efficiency η of a TEM is defined as the ratio between electric power output P and the incident heat flow at the hot side of a TEM Q_{in} .

$$\eta = \frac{P}{Q_{in}} \quad (1)$$

The maximum conversion efficiency η_{MAX} is determined by the Carnot efficiency $\eta_C = (T_H - T_C)/T_H$, which depends on the hot side temperature T_H and cold side temperature T_C at the TEM. Loss mechanisms and thermoelectric (TE) material properties affect η_{MAX} by the module's figure of merit $ZT_{TEM} = S^2/(R_i \cdot K) \cdot T_m$ additionally. ZT_{TEM} is defined by the effective value of the Seebeck coefficient S , the thermal conductance K , and the electric resistance R_i of the module with respect to the temperature range of operation and the corresponding mean temperature $T_m = (T_H - T_C)/2$ [9].

$$\eta_{MAX} = \frac{T_H - T_C}{T_H} \frac{\sqrt{1 + ZT_{TEM}} - 1}{\sqrt{1 + ZT_{TEM}} + \frac{T_C}{T_H}} \quad (2)$$

Improvement of high temperature TE material performance and continuous scientific and technological progress on contacting technologies revealed mature prototypes [10,11,12] and led to releases of small batch productions by industries [13,14,15,16]. TEM efficiencies between 8.9% [17] and 12% [18] could be shown in dependence of the chosen TE material. A precise characterization of TEM becomes increasingly important in view of this progress, since a development of markets for TE applications and a successful industrialization must be supported by the availability of traceable metrology with defined uncertainty budgets for provision of reliable module specifications, definition of installation instructions and information on the expected operation life time or degradation rate, respectively.

Due to the lack of guidelines and standards for testing methods the reliable specification of the TEM properties, which is ultimately connected to the expression of measurement uncertainties, has remained challenging to date. The provision of conclusive data for the quantification of uncertainty

budgets requires elaborate repetitive experiments in order to identify relevant metrological influencing parameters for a wide set of measurands within a statistically meaningful range of measurement boundary conditions. Inter-laboratory comparisons of measurement data obtained on comparative TEM samples represent an effective way to determine result deviations and to assess the reliability of employed facilities by only a limited number of measurements with manageable effort.

High precision characterization methods have to be developed and qualified as primary methods. Their results enable the qualification of TEM reference samples with low uncertainties, which are still missing up to now. Respective work on high temperature reference TEM has been already started [19,20] and will pave the way to quantify uncertainty budgets of used measurement techniques in future. Meanwhile commercial TEM, which are mainly available as Bi_2Te_3 -based devices, could serve as reference samples, too. Bi_2Te_3 and its solid solutions with antimony and selenium represent a known TE material class, which is widely used since decades for industrial productions of TEM devices worldwide [21,22,23,24,25,26,27]. This material class offers a decent device efficiency of up to 7.2% [28] but can be only applied to maximum temperatures below 327°C [21] due to the material stability of Bi_2Te_3 . Several works have been accomplished in order to protect this material from oxidation by application of coatings [29] and to increase its temperature stability by means of annealing techniques [30,31,32] or compositional modification by addition of elements [33,34,35]. Though ZT-values > 1 have been published even up to temperatures of 500°C [36] the maximum application limit of commercial Bi_2Te_3 -based TEM devices remained practically below 300°C [37]. However, as long as certified reference TEMs are not available, commercial Bi_2Te_3 -based TEM represent the best alternative for metrological investigations.

According to requirements on the qualification of reference samples [38] the functional stability and similarity (homogeneity) of TEMs have to be proven in first place. As long as temperature dependent functional properties coincide with representative TEM characteristics, a maximized performance (power output, efficiency) plays only a secondary role for reference modules. Even reversed, it might be beneficial for the case of a metrological reference module to base on a mature TEM technology with only moderate module performance in favour of a possibly lower functional degradation, which in turn would yield low uncertainties and longer utilization periods of qualified reference samples.

Investigations on Bi_2Te_3 -based TEMs from four different industrial manufacturers are reported in this work including the derivation of the uncertainty budget for the determination of the internal electric resistance R_i . The modules have been tested initially under variable mechanical pressure conditions and constant temperature differences of 150°C or 175°C, respectively. In order to assess functional stabilities thermal cycling experiments have been performed subsequently on the hot side temperature between 100°C/125°C and 200°C/225°C/250°C in dependence of the module type. The pressure sensitivity of each module type was assessed by changes of R_i , while the evolution of R_i in response to cyclic thermal loads served for the evaluation of short- and long-time stabilities. Two module types with superior stability proceeded to additional tests regarding their homogeneity (similarity of R_i).

Due to a too short observation time (long time stability) and limited sample number (homogeneity) the extent of measurements performed in this work does not fulfil legal requirements, which are formulated for the certification of reference samples by applicable provisions of the International Organization for Standardization (ISO) within the ISO-Guide 35 [38]. However, the reported work

represents a step towards the yearned standardization of TEM metrology and pursues the central aim of the qualification of suitable comparative samples for later inter-laboratory tests. TEM round robin tests shall be conducted among renowned thermoelectric laboratories for the first time and will be reported in a subsequent publication. Hereby characterization of TEM modules will perspectively catch up the significantly advanced level of metrological standardization of TE material characterization, which is given by available reference samples for integral measurements of the Seebeck coefficient [39,40], publications on best practice measurement approaches [41,42], and accomplished international round robin campaigns on transport property measurements [43,44,45].

2. Experimental

Section 2.1 starts with a brief survey on the custom-made characterization facility “*TEGMA*” (Thermoelectric Generator Measurement Apparatus), which is operated at DLR. Herein we report basic device specifications only, while a detailed description of this apparatus has been reported together with underlying characterization methods in a previous work [46]. However, the uncertainty of the measurement of R_i is derived in detail within section 2.2, too, since it has a strong relevance for the discussion of results of the conducted test program. Basic information on the investigated TEMs and details about the conducted test program are presented in the following sections 2.3 and 2.4, respectively.

2.1 Thermoelectric Generator Measurement Apparatus

The TEGMA (Figure 2) offers a fully automated TEM characterization under application conditions. It consists of a vacuum recipient, a control cabinet, a linear actuator (Mini3, Framo Morat) for pressure adjustment, and an external chiller (Unistat 815, Huber) for the rejection of heat at the cold side of the measuring section. Besides other components, the control cabinet accommodates a DC-power supply (XKW150-20, Xantrex) for the used heater and a Proportional-Integral-Differential (PID) temperature controller (2216e, Eurotherm) in order to adjust thermal conditions during TEM experiments.

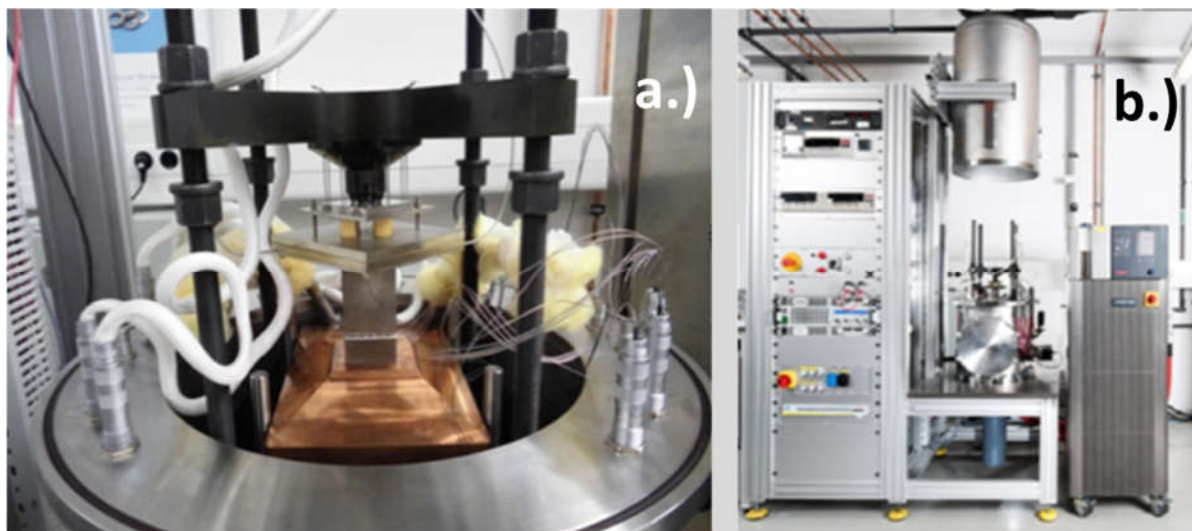


Figure 2: Measuring Section (a) of the TEM characterization facility “*TEGMA*” (b) at DLR.

The electric characterization is accomplished by means of a DC electronic load (EA-EL 9400-50, Elektro-Automatik), which is connected to the terminals of the TEM for adjustment of the load

current I . The TEM current I is determined by a measurement of the voltage drop V_{ref} over a shunt resistor $R_{\text{ref}} = 0.1 \, \Omega$ (PBV0.1, Isabellenhütte) with a low tolerance of $\pm 0.5\%$ [47]. Voltages and signals from temperature sensors are fed to a multiplexer card (7708, Keithley). The multiplexer is integrated within a digital multimeter (DMM 2700, Keithley), which offers an accuracy of $\pm (30 \text{ ppm of reading} + 5 \text{ ppm of range})$ [48]. Considering a rectangular probability distribution within this interval leads to following maximum uncertainties in dependence of the available range settings of this DMM (Table 1).

Table 1: Maximum standard measurement uncertainties for direct current (DC) voltage measurements of the Keithley 2700 DMM in dependence of its range settings. The uncertainty for the 1000 V input range is omitted due to missing relevance.

Range	100 mV	1V	10V	100V
$u(V)$	$\pm 2.02 \, \mu\text{V}$	$\pm 20.2 \, \mu\text{V}$	$\pm 202 \, \mu\text{V}$	$\pm 2.02 \, \text{mV}$

The TEGMA uses a heating wire inside an Inconel heating plate to provide the heat flow to the measuring section. The heat flow is removed from the measuring section by a cooling plate, which is connected to the external chiller. The measuring section consists of an oxygen-free Cu heat exchanger, which is placed between the heater and the TEM, and an oxygen-free Cu heat flow meter (HFM) located between the TEM and the cooling plate (Figure 3).

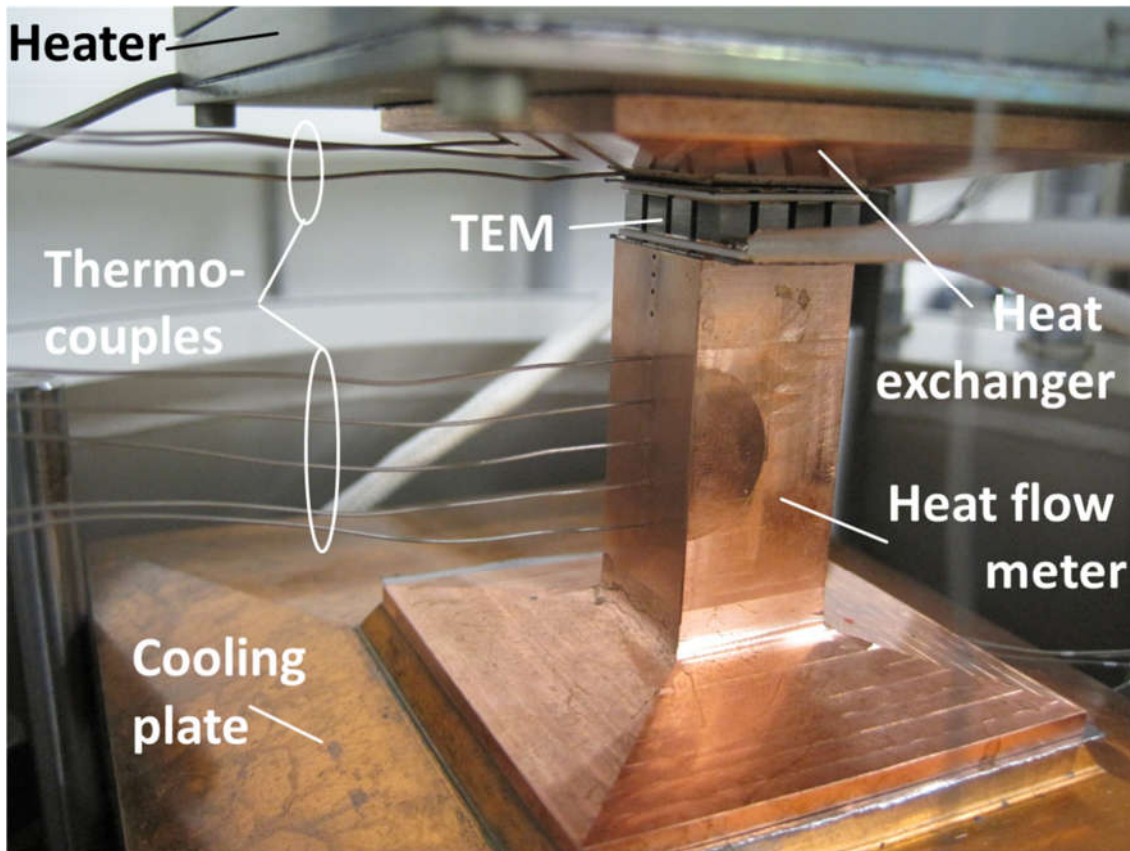


Figure 3: Measuring section of the TEGMA facility for TEM characterization prior to its thermal damping.

Five type-N thermocouples (0.5 mm diameter, Inconel sheath, 1NI05/1000/MP/FM.N, ThermoExpert) are placed along the central axis of the HFM. The sensors measure the cold side

temperature T_C at the TEM by an extrapolation technique. The hot side temperature T_H of the TEM is obtained from three sensors (same type as for the HFM), which are placed along the central axis of the hot side heat exchanger.

A 0.2 mm thick graphite foil (Dr. Fritsch Sondermaschinen GmbH) is used for thermal coupling between all parts of the measuring section (heater, heat exchanger, TEM, heat flow meter, cooling plate). New foils are used at every sample installation. The measuring section is mechanically loaded by a linear actuator, which provides an axial pressure on the column in order to reduce thermal contact resistances between the stacked components. The force is transmitted by a spring package underneath the cooling plate (Figure 4b). These springs reduce pressure variations during thermal cycling of samples, which could occur due to a thermal expansion of involved components within the stack. The force is measured by a strain gauge force transducer (C9B, HBM), which is regularly calibrated against an in-house calibration standard (Figure 4a).

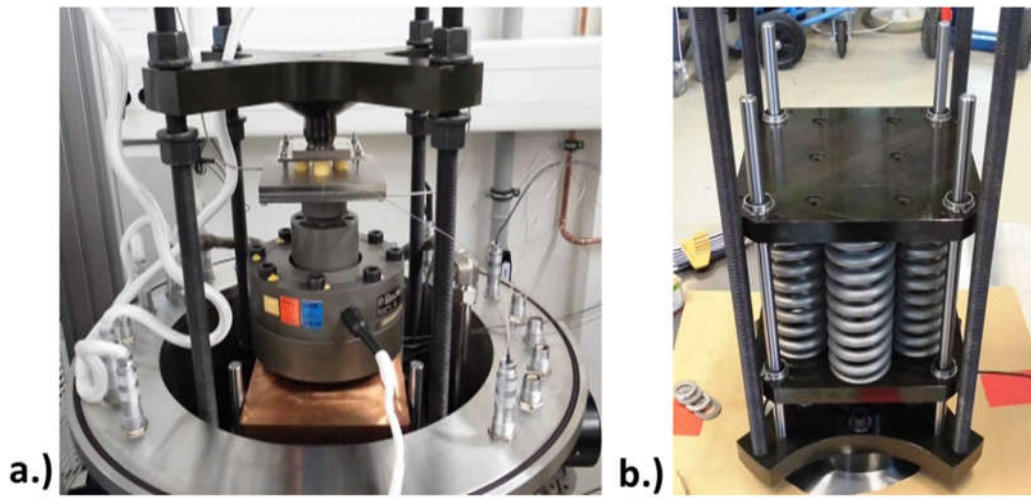


Figure 4: Calibration of the force sensor at the TEGMA facility against an in-house calibration standard (a). A spring package (b) is installed underneath the cooling plate. The springs apply a force on the TEM and reduce undesired pressure changes during measurements, which could be caused by thermal expansion of components in the force transmission path.

Temperatures at the hot and cold side of the TEM are adjusted by means of respective set points for the temperatures of the heater and the cooling plate. The open loop voltage V_0 is measured after temperature stabilization. V_0 is determined by the number of thermocouples N_{pn} within the TEM, the effective Seebeck coefficient per thermocouple S_{eff} and the present temperature difference ΔT .

$$V_0 = N_{pn} \cdot S_{eff} \cdot \Delta T = N_{pn} \cdot S_{eff} \cdot (T_H - T_C) \quad (3)$$

Following the measurement of V_0 an electric direct current (DC) through the TEM is adjusted, which alters the temperature conditions due to the Peltier effect [49]. The entire current range is typically chosen from open loop ($I = 0$ A) up to the short circuit current I_{SC} . I_{SC} depends on the temperature conditions and is characteristic for each TEM sample type. Both values, the current I and the terminal voltage V are measured twenty times at every current set point in order to calculate measurement uncertainties and mean values, which average out the impact of statistical signal noise.

Evaluation of the resulting I - V -characteristic (Figure 5) gives access to the internal electric resistance R_i of the module. R_i is measured at DLR by means of a Rapid-Steady-State (RSS) method [46] in order to compensate the decreasing open loop voltage $V_0^*(I)$ with increasing current flow. This approach avoids an overestimation of R_i , which would occur at fixed heater and cooler temperatures by a

direct evaluation of the slope $\Delta V/\Delta I$. The reduction of $V_0^*(I)$ is attributed to the decreasing temperature difference across the TEM due to the transported Peltier heat, which is proportional to the electric current flow [49]. R_i is evaluated at different electric currents from differences between steady state terminal voltages $V(I)$ and corresponding values of the reduced open loop voltage $V_0^*(I)$. The procedure is described in detail within Ref. 46.

$$\Delta V_1 = V|_{I_1 \rightarrow 0} - V|_{I=I_1} = V_0^*(I_1) - V(I_1) = V_{0,1} - V_1$$

$$\Delta V_2 = V|_{I_2 \rightarrow 0} - V|_{I=I_2} = V_0^*(I_2) - V(I_2) = V_{0,2} - V_2$$

$$R_i = \frac{\Delta V_1 - \Delta V_2}{I_1 - I_2} = \frac{V_{0,1} - V_1 - V_{0,2} + V_2}{I_1 - I_2} \quad (4)$$

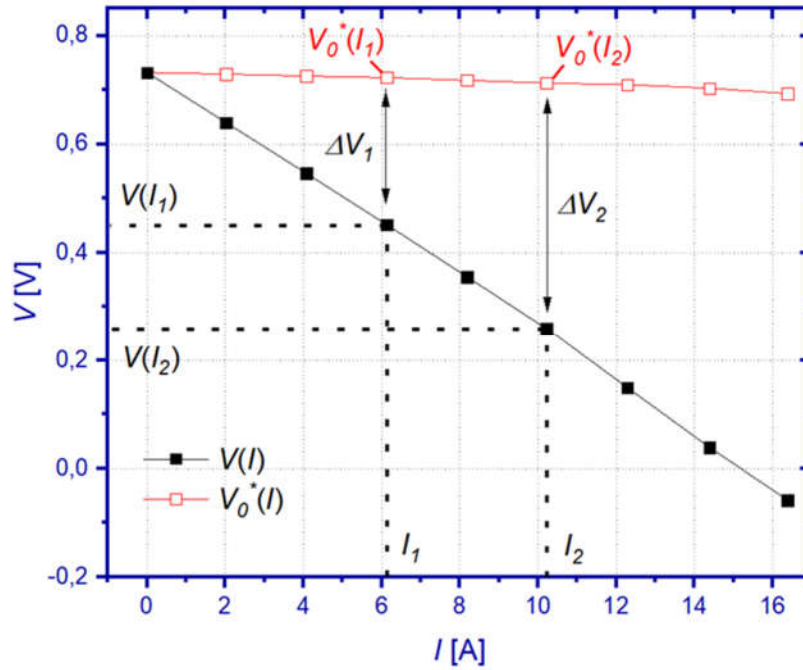


Figure 5: The I - V curve shows the terminal voltage V at the TEM as a function of the current flow I (full black symbols) at fixed heater and cooler temperatures. The Peltier effect causes a decreasing temperature difference at the TEM and lowered open circuit voltage $V_0^*(I)$ (blank red symbols) with increasing current flow as a result of the limited thermal conductance of the heat transferring components in series to the TEM.

2.2 Uncertainty of electric resistance measurements

In accordance to the “*Guide to the expression of uncertainty in measurement*” (GUM) [50] the combined uncertainty $u(R_i)$ is determined from a geometric sum of terms, which represent individual uncertainty contributions of every input variable of equation 4. Every term consists of a product of the standard measurement uncertainty u and the corresponding sensitivity coefficient c of a particular input variable.

$$u(R_i) = \sqrt{c_{V_1}^2 u(V_1)^2 + c_{V_{0,1}}^2 u(V_{0,1})^2 + c_{V_2}^2 u(V_2)^2 + c_{V_{0,2}}^2 u(V_{0,2})^2 + c_{I_1}^2 u(I_1)^2 + c_{I_2}^2 u(I_2)^2} \quad (5)$$

The sensitivity coefficients c can be determined from partial derivatives of the measuring function (equation 4) with respect to the actual input variable.

$$c_{V_1} = \frac{dR_i}{dV_1} = \frac{1}{I_1 - I_2} \quad (6)$$

$$c_{V_2} = \frac{dR_i}{dV_2} = \frac{1}{I_1 - I_2} \quad (7)$$

$$c_{V_{0,1}} = \frac{dR_i}{dV_{0,1}} = \frac{1}{I_1 - I_2} \quad (8)$$

$$c_{V_{0,2}} = \frac{dR_i}{dV_{0,2}} = \frac{1}{I_1 - I_2} \quad (9)$$

$$c_{I_1} = \frac{dR_i}{dI_1} = -\frac{\Delta V_1 - \Delta V_2}{(I_1 - I_2)^2} \quad (10)$$

$$c_{I_2} = \frac{dR_i}{dI_2} = \frac{\Delta V_1 - \Delta V_2}{(I_1 - I_2)^2} \quad (11)$$

Here, I_1 , I_2 , ΔV_1 , and ΔV_2 denote best estimates of every measured value. Every estimate equals the expectation (mean) value of the respective result distribution, which forms from the number of captured signal readings. Standard uncertainties for voltage measurements $u(V_1)$, $u(V_{0,1})$, $u(V_2)$, $u(V_{0,2})$ are either equal to the measurement uncertainty of the used digital multimeter ($\pm 0.5 \mu V$) or relate to the distribution width of the recorded readings, whichever is greater. Such distributions can stem from signal fluctuations due to statistic noise, temperature variations and fitting errors during the processing of transient voltage signals according to the RSS-method. If result distributions become broader than expectable from the uncertainty of the DMM, which is the regular case here, standard uncertainties are calculated for Gaussian result distributions according to equation 12, which is based on the full width at half maximum value (FWHM) of a respective set of values.

$$u = \frac{FWHM}{2 \cdot \sqrt{2} \cdot \ln 2} \quad (12)$$

If result distributions do not show a Gaussian but random distribution, the uncertainty of a measurement is calculated on the base of the empiric standard deviation s [50,51].

$$s = \sqrt{\frac{1}{N-1} \sum_{i=1}^N (V_j - \bar{V})^2} \quad (13)$$

Herein, N denote the number of readings (in this study $N = 20$), V_j is the value of the j^{th} reading, while \bar{V} is the mean value of all readings. According to equation 14 the standard deviation s gives access to the standard uncertainty u of a measurement.

$$u = \frac{s}{\sqrt{N}} \quad (14)$$

The measurement function of the TEM current I is given by equation 15, in which V_{Ref} represents the voltage drop over the shunt resistor R_{Ref} .

$$I = \frac{V_{\text{Ref}}}{R_{\text{Ref}}} \quad (15)$$

The uncertainty of the current measurement $u(I)$ is calculated as a combined uncertainty within a sub-model. It consists of uncertainty contributions from the voltage measurement V_{Ref} and the contribution due to the tolerance of the shunt resistor R_{Ref} .

$$u(I) = \sqrt{c_{V_{\text{Ref}}}^2 u(V_{\text{Ref}})^2 + c_{R_{\text{Ref}}}^2 u(R_{\text{Ref}})^2} \quad (16)$$

$$c_{V_{Ref}} = \frac{dI}{dV_{Ref}} = \frac{1}{R_{Ref}} \quad (17)$$

$$c_R = \frac{dI}{dR_{Ref}} = -\frac{V_{Ref}}{(R_{Ref})^2} \quad (18)$$

Sensitivity coefficients are calculated again from partial derivatives of the underlying measurement function (equation 15). The best estimate for V_{Ref} and the standard uncertainty $u(V_{Ref})$ is determined analogous to the above described voltage uncertainties. The best estimate $R_{Ref} = 0.1 \text{ m}\Omega$, while its standard uncertainty $u(R_{Ref}) = 0.5 \text{ m}\Omega$ in accordance to the specified resistor tolerance.

A single and universal value cannot be expressed for $u(R_i)$ due to its dependence on voltage and current ranges, which are individual for every module type and correlated to measurement boundary conditions. With anticipation of characterization results obtained on the first set of tested TEMs during the initial measurement M01 (Table 4) the following table 2 summarizes the quantitative evaluation of $u(R_i)$ according to equation 5. Additional information on best estimates, sensitivity coefficients and individual uncertainty contributions are given for every input variable within the supplementary information Table S1 of this article (“S” denotes a supplementary information).

Table 2: Characterization results of the first module measurement M01 (refer to Table 4) with measured value of R_i and resulting uncertainties $u(R_i)$ according to equation 5. Uncertainties are shown for every module by an absolute value and relatively to R_i .

Module type	A	B	C	D
R_i from M01 [Ω]	3.58	2.15	22.74	0.74
$u(R_i)$ [$\text{m}\Omega$]	55.51	32.69	219.68	16.89
$u(R_i)$ [%]	1.55	1.52	0.96	2.28

2.3 Thermoelectric Generator Modules

Four types of Bi_2Te_3 -based thermoelectric generator modules have been chosen for the tests. Every module is offered as a regular product by a different manufacturer. Table 3 summarizes available information and product specifications.

Table 3: Information about the tested modules is taken from manufacturer specifications. Module type C was purchased from a distributor. The place of manufacturing is unknown for this type. The given geometry data does not refer to the overall dimensions of the modules but to the cross-section area, which is available for thermal coupling (active area). The nominal hot and cold side temperatures T_h and T_c refer to testing conditions of specified module properties.

Module type	A	B	C	D
Place of manufacturing	USA	Japan	Unknown	China
Geometry [mm^3]	40x40x3.5	51.5x51.5x4.5	54x54x3.4	50x50x3.5

Maximum T_h [°C]	230	280	200	200
Nominal T_h [°C]	230	280	175	200
Nominal T_c [°C]	50	30	50	35
R_i [Ω]	3.46	1.15 (@ 27°C)	20	0.67
Maximum P [W]	7.95	24	6.8	Unknown
Maximum η [%]	4.97	7.2	Unknown	Unknown

2.4 Test program

Initially one module from each TEM type was tested under a variable mechanical pressure p between 2 MPa and 3.5 MPa (M01 – M04) in order to determine the involved sensitivity of R_i . The selected pressure range did not account for lower values between 0.1 – 1 MPa, since Type A modules require a minimum pressure of 2 MPa according to rated manufacturer specifications. To avoid a changing impact of the thermal coupling resistance between the modules and the measurement configuration, higher pressure levels between 2 MPa and 3 MPa have been applied during tests in order to obtain comparable conditions at the module boundary surfaces for every tested TEM type. However, it can be assumed that the pressure sensitivity of R_i would be higher with decreasing pressure level, which could increase observable deviations during inter-laboratory data comparisons due to uncertainties connected to the setting and control of effective axial pressure. These tests were conducted at a constant cold side temperature $T_c = 50^\circ\text{C}$ and in dependence of the module type at constant temperature differences $\Delta T = 150^\circ\text{C}$ and 175°C , respectively. Weak or unstable electric contacts within TEM can be occasionally identified by the pressure sensitivity of R_i . Apart from an assessment of the contact stability these tests should quantify the possible impact of uncertainties during pressure settings, which might occur in later comparative measurements in the course of a round robin test and could contribute to observable deviations of different measurands among participating laboratories, too.

The short-term stability was tested subsequently on the same set of modules but after a reinstallation with the use of new graphite foils for thermal coupling of components within the measuring section. These tests have been conducted at 3 MPa and at a constant cold side temperature of 50°C . The hot side temperature was cycled several times (M05 – M09) between 100°C / 125°C and respective maximum application temperatures for continuous operation. During tests of the pressure sensitivity and the short-term stability investigation the temperature stabilization time was set relatively to the remaining temperature drift at the TEM, which was limited to a maximum value of 0.15 K/min. Once a particular temperature set point stabilized, determination of the open loop voltage V_0 initiated the measurement of the I/V -characteristic in order to determine R_i . The current I was adjusted in nine steps between open loop and short circuit conditions. At each of the current set points the same temperature stabilization criterion (maximum drift of 0.15 K/min)

had to be met prior to the measurement of the terminal voltage V and the current-dependent open loop voltage $V_o^*(I)$ for determination of R_i (equation 4).

The long-term stability was tested on a second set of modules (one from each type) in a next step (M10). These measurements were conducted at 3 MPa and at a constant cold side temperature $T_c = 50^\circ\text{C}$. The hot side temperature T_h was cycled between 125°C and 225°C for type A and B modules, while other types were cycled between 100°C and 200°C . The lowered hot side temperature for the second group was chosen since results from M05-M09 revealed a worse functional stability for these TEM types. During long-term stability investigations the temperature stabilization time was set to 20 minutes at every temperature set point. The measurement of R_i (equation 4) was accomplished by only three current set points per temperature step, effectively quartering the current range between open loop and short circuit conditions. The stabilization time after each current change was set to 10 minutes. In contrast to the setting of a maximum temperature drift this procedure was chosen in order to maximize the number of hot temperature cycles within a given time.

After the long-term stability measurement further homogeneity tests (M11) were carried out on a third module set with modules of type A and B only due to their superior stability. The third set comprised three additional modules of both types, which were characterized at $T_c = 50^\circ\text{C}$, while one temperature cycle was performed at the hot side between 100°C and 200°C . Table 4 summarizes the test program and gives an overview on the respective measurement conditions, number of temperature cycles, and duration of each run.

Table 4: Test program overview.

Measurement	M01 – M04 (Pressure)				M05 – M09 (Short-term)				M10 (Long-term)				M11 (Homogeneity)	
Module type	A	B	C	D	A	B	C	D	A	B	C	D	A	B
T_h set points [°C]	225		200		125 175 225	100 150 200 250	100 150 200		125 175 225		100 150 200		100 150 200	
T_c set point [°C]	50													
Pressure set points p [MPa]	2 → 2.5 → 3 → 3.5				3									
Number of cycles of T_h	0 - constant ΔT				3	3	2	3	119	41	151	98	1	1
Duration per TEM [h]	12	9	13	12.5	54	60	41	47	330	117	443	253	17	18
Module set / TEMs per type	1 st / 1								2 nd / 1				3 rd / 3	

3. Test results

3.1 Pressure tests (M01-M04)

The efficiency of a TEG is determined by the effective temperature difference across the installed TE materials. Any parasitic temperature drop along the heat transmission path between the heat source and the heat sink lowers the performance of a TEG. Therefore, TEMs are usually clamped under mechanical pressure between heat exchanging components with the use of thermal interface materials (TIM) in order to reduce thermal contact resistances at the boundaries of a TEM. With regard to individual solutions for a TEG-system assembly several references point out to the impact of the applied mechanical pressure on the system performance [52,53,54] and the suitability of different TIMs like foils, greases, multi wall carbon nano tubes or copper particles [55,56,57]. The mentioned works [52,53,54] tested the pressure impact on ΔT and provided discussions on resulting changes of the electric power output. Due to the impact of the applied pressure on functional TEM properties their sensitivity must be characterized not only for a design optimization of an application system but likewise for the qualification of a metrological TEM reference sample, since it might indicate a lacking parallelism of the TEM coupling faces (changing ΔT) or a weak or unstable electrical coupling within a TEM (changing R_i). In order to reduce the impact of uncertainties of pressure settings on measurand comparisons in the course of a later round robin campaign, a module type with a preferably low or moderate pressure dependency of its properties should be chosen as a test sample. However, apart from the question of the pressure impact on the external thermal coupling of a TEM the applied pressure might have an effect on internal electric contact resistances, too, which are governed by the quality and stability of multiple interfaces between metallic bridges and TE legs (Figure 1). To the best of our knowledge a discussion on a pressure-induced change of R_i was not documented in literature before.

Figure 6 shows the outcome of the pressure sensitivity of R_i , which was tested in the course of M01-M04 on the first set of TEM samples. From expectation R_i should decrease with increasing pressure, since possibly existing cavities at the interfaces between metallic bridges and TE-legs could be successively closed.

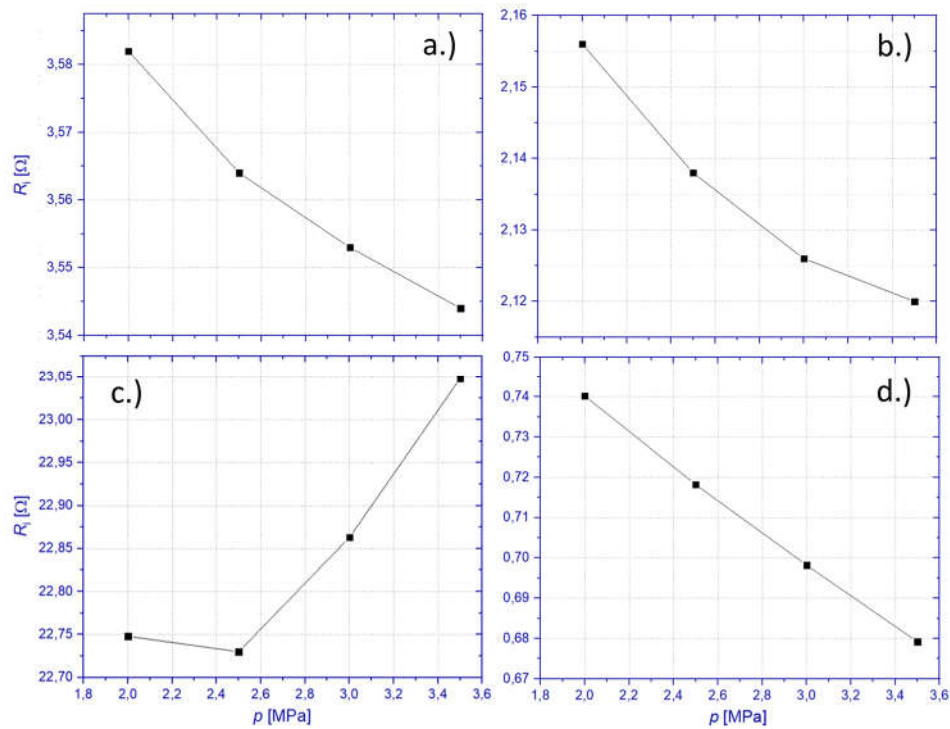


Figure 6: The pressure sensitivity of R_i characterized during M01-M04 for different modules types (a. - Type A, b. - Type B, c. - Type C, d. - Type D).

Except for the module type C this trend was confirmed for every other tested type. The increasing R_i of type C does not stem from a pressure influence but most likely from a temperature-induced module degradation, as will be shown later (section 3.2). However, qualitative differences could be likewise observed among the other module types. While modules A and B showed first signs of a saturation of the pressure dependency of R_i at highest loads, this was not observed for type D, which revealed a linear trend over the entire pressure range.

Table 5 summarizes the outcome of the pressure tests on R_i . As can be seen modules of types A and B showed lowest absolute changes of R_i and, when neglecting results of type C due to its supposed functional instability, minimum relative changes, too.

Table 5: Maximum change of R_i within a pressure interval of 1.5 MPa. The data reflects maximum absolute changes and relative differences in relation to starting values of R_i at 2 MPa.

Module type	A	B	C	D
ΔR_i [mΩ]	-38	-36	+300	-61
ΔR_i [%]	-1.07	-1.67	+1.32	-8.68

Clear trends could be observed for the pressure dependencies of R_i . However, maximum values of ΔR_i in Table 5 have to be set into relation to the measurement uncertainty of $u(R_i)$, which is given in Table 2. This comparison confirms that ΔR_i remained within the measurement uncertainty only for the type A module, while it exceeded $u(R_i)$ only by 4 mΩ for the type B module. Although reasonable

pressure dependencies of R_i have been obtained for these two module types, quantification of a pressure induced change of R_i cannot be given without doubt. For module types C and D ΔR_i exceeded $u(R_i)$ significantly, which confirms at least a causal pressure influence.

For the sake of completeness, further results of M01-M04 have been summarized within the supplementary information S2. Figures in S2 show additionally the open loop voltage V_o , heat flow Q (at open loop conditions), maximum power output P_{Max} , and maximum efficiency η_{Max} in dependence of the applied pressure. It should be noted here, that this evaluation revealed distinct differences compared to specified performance key figures, which have been claimed by the manufacturers. These differences can be either caused by unknown uncertainty budgets of the employed characterization techniques for module specification or fundamental deviations with regard to TEM installation and boundary conditions. A clarifying analysis is not feasible yet due to unknown details of the utilized characterization techniques, which are operated by manufacturers. However, the result comparison given by S2 confirms the high module quality of type A and B TEMs with regard to their superior module efficiencies.

3.2 Short-term stability (M05-M09)

The degradation of functional TEM properties is a complex and ongoing field of research, which gave proof of a variety of possible reasons for module deterioration like for instance thermo-mechanically induced contact failure [58,59,60], material evaporation [61], oxidation [62], evolution of microstructures and phase transformations [63,64] or contact diffusion [65,66,67]. However, most of the reported investigations on TEM stability point out to temperature-induced module degradation mechanisms. The stability of functional properties is one of the most important features of reference samples, since it builds the base for meaningful device tests and valid calibration procedures. Therefore, in extreme cases reference samples must comply with property specifications at least for the duration of a single measurement, which is assured in principle once a sufficient short-term stability can be proven. All modules from the first set have been cycled on the hot side temperature up to three times (M05-M09), in order to reproduce a typical sample utilization for the duration of a single measurement with a low number of repetitive thermal cycles. Results of these experiments are displayed within Figures 6 – 9 together with the temperature profiles for M01-M09. A detailed quantitative evaluation of M05-M09 can be found in S3 within the supplementary information of this article. Tables in S3 comprise evaluations of temperature dependent mean values of R_i , corresponding standard deviations $\sigma(R_i)$ and maximum observable changes ΔR_i .

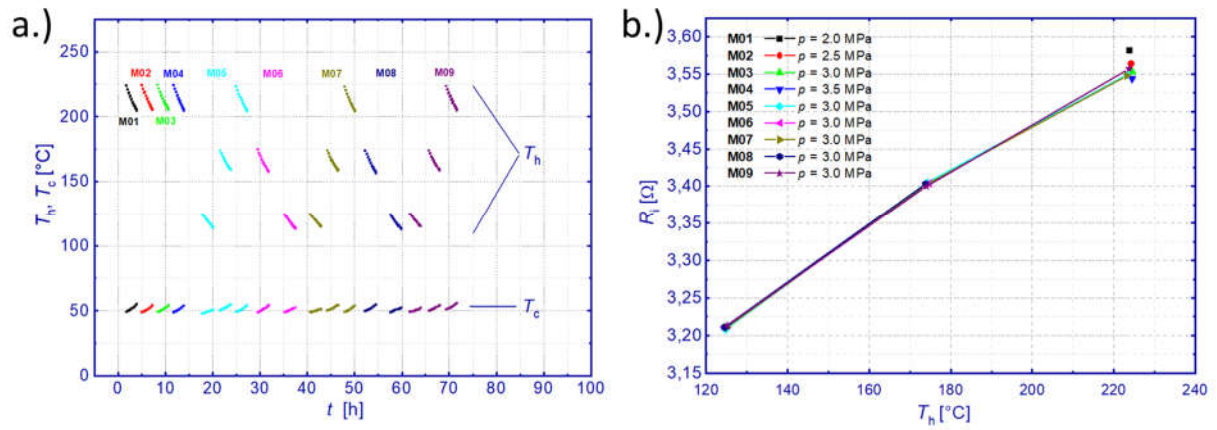


Figure 7: Temperature history (a) and evolution of the temperature dependent electric resistance R_i (b) of module type A in the course of measurements M01 – M09.

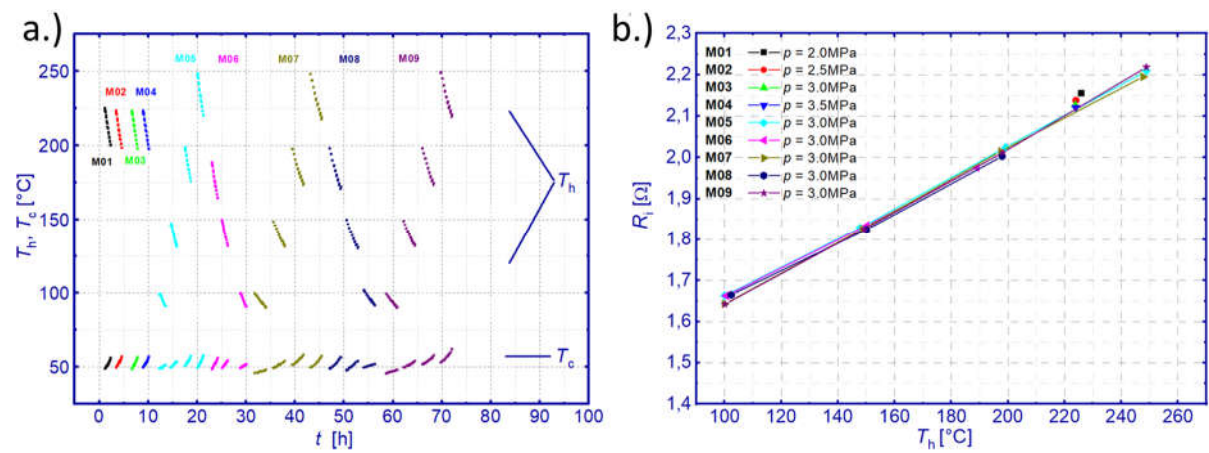


Figure 8: Temperature history (a) and evolution of the temperature dependent electric resistance R_i (b) of module type B in the course of measurements M01 – M09.

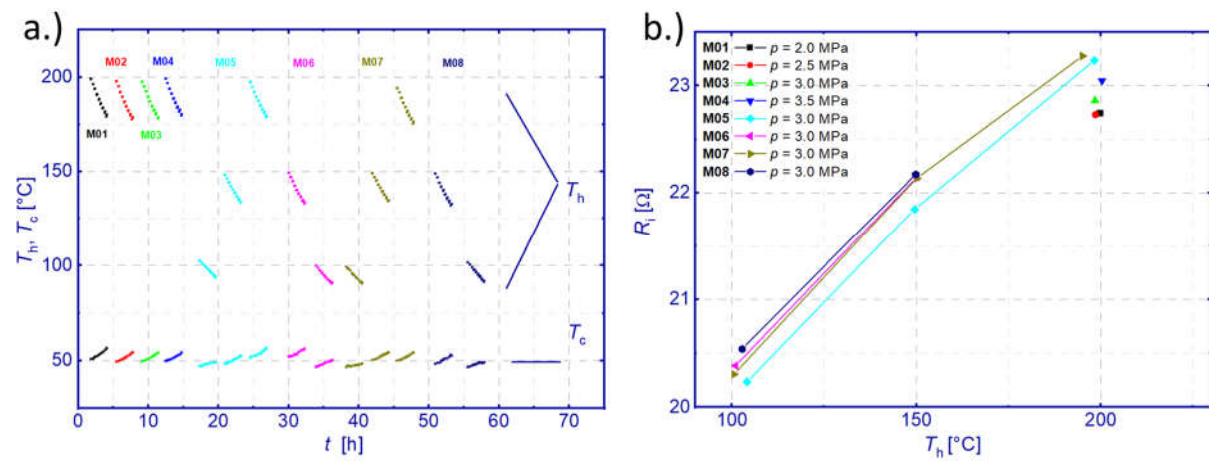


Figure 9: Temperature history (a) and evolution of the temperature dependent electric resistance R_i (b) of module type C in the course of measurements M01 – M08.

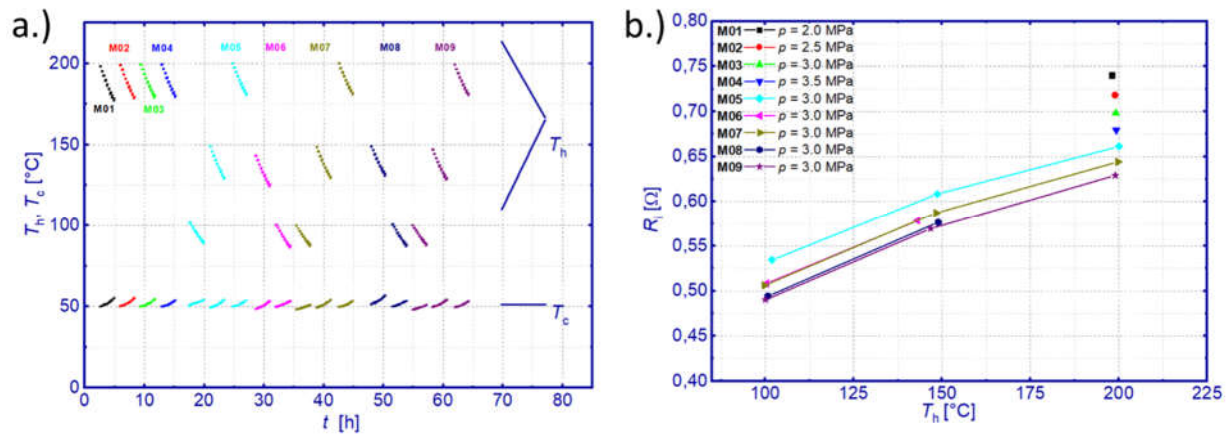


Figure 10: Temperature history (a) and evolution of the temperature dependent electric resistance R_i (b) of module type D in the course of measurements M01 – M09.

Table 6 shows a summary of the evaluation of the short-term stability test. The displayed standard deviations have been averaged from temperature dependent data, which is given in Tables S3.

Table 6: The absolute and relative standard deviation $\overline{\sigma(R_i)}$ was averaged from temperature dependent values (Tables S3), which were obtained from results of R_i during M05-M09. The maximum change ΔR_i reflects the maximum observable difference of R_i at any temperature T_H . The relative value of ΔR_i gives the maximum change in relation to the mean value of R_i .

Module type	A	B	C	D
$\overline{\sigma(R_i)}$ [m Ω]	2.88	11.48	104.9	16.1
$\overline{\sigma(R_i)}$ [%]	0.08	0.59	0.49	2.82
max. ΔR_i [m Ω]	9	23	329	44
max. ΔR_i [%]	0.253	1.33	1.49	8.68

Type A and B modules revealed an excellent stability of R_i . For type A changes of R_i lead to a maximum standard deviation $\sigma(R_i) < 5$ m Ω at $T_H = 225^{\circ}\text{C}$, which equals less than 0.14% of the respective mean value of R_i at this temperature (Table S3-1). Even lower deviations could be observed for the type A module at lower temperatures. Overall, the mean standard deviation over the entire temperature range was $\sigma(R_i) = 2.88$ m Ω corresponding to an averaged relative standard deviation of 0.08% (Table 6), which is far below the measurement uncertainty of 1.55% (Table 2). Even maximum changes ΔR_i stayed significantly below the uncertainty limit for type A module. The type B module showed slightly higher absolute standard deviations at $T_H = 100^{\circ}\text{C}$ and $T_H = 250^{\circ}\text{C}$ of approximately 11.6 m Ω , which corresponds to 0.7% and 0.5% of the mean value at respective temperatures (Table S3-2). At intermediate temperatures $T_H = 150^{\circ}\text{C}$ and $T_H = 200^{\circ}\text{C}$ the deviation of R_i was 4 m Ω and 9 m Ω , which equals 0.2% and 0.45% of the mean values of R_i at these temperatures. Overall, the mean standard deviation for the type B module was $\sigma(R_i) = 11.48$ m Ω

over the entire temperature range corresponding to an averaged relative standard deviation of 0.59% (Table 6), which is within approximately 40% of the measurement uncertainty of 1.52% (Table 2). Maximum changes ΔR_i of the type B module stayed within the uncertainty limit, too.

Type C and D modules revealed a continuous change of R_i but with reverse signs of their evolutions. Similarly, as for the tests with varying pressure but constant temperature differences (M01-M04) R_i showed a continued monotonous increase for type C and a decrease for type D at constant pressure but varying temperature differences in the course of M05-M09. Although standard deviations (Table 6) kept within the uncertainty budgets and change rates of R_i seem to reduce over the number of temperature cycles, it becomes apparent from Figures 9b and 10b that R_i of module types C and D is not stable under the tested conditions. While changes of R_i could be caused by the varying pressure and/or the temperature impact during M01-M04, results from M05-M09 suggest that the observed change of R_i is mainly caused by the temperature impact. Further tests would be necessary to clarify whether the change of R_i is caused dominantly by the holding time at elevated hot side temperature or by effects from cyclic thermal conditions. During the short-term stability test the type C module showed a maximum standard deviation $\sigma(R_i) < 155 \text{ m}\Omega$ at $T_H = 150^\circ\text{C}$ corresponding to 0.7% of the respective mean value (Table S3-3). This is still within the measurement uncertainty of 0.96% (Table 2). However, the corresponding maximum change of R_i was determined for this module type with $\Delta R_i = 329 \text{ m}\Omega$ (Table 6). This equals a relative difference to the mean value of 1.49%, which lies above the measurement uncertainty and confirms a module degradation. Same holds for the type D module, which showed a maximum standard deviation $\sigma(R_i) < 17.23 \text{ m}\Omega$ at $T_H = 100^\circ\text{C}$ corresponding to 3.4% of the respective mean value (Table S3-4). This standard deviation already exceeds the measurement uncertainty budget, which was specified for module type D $u(R_i) = 2.28\%$ (Table 2). The maximum change of R_i was determined for this module type with $\Delta R_i = 44 \text{ m}\Omega$ (Table 6). This equals a relative difference to the mean value of 8.7%, which lies significantly above the measurement uncertainty effectively confirming a functional instability of the type D module under the tested conditions.

3.3 Long-term stability (M10)

Practically and from an economic point of view reference samples have to offer stable properties with low uncertainties not only for the duration of a single test but for longer periods or series of measurements, in order represent convenient solutions for daily laboratory practise. This quality is ensured by tests of the long-term stability, which have been conducted on a second set of modules (one from each type). The following Figures 11-14 show the respective temperature profiles and the evolution of R_i for each module type in response to the applied cyclic thermal load. A detailed quantitative evaluation of M10 can be found in S4 within the supplementary information of this article. Tables in S4 comprise evaluations of temperature dependent mean values of R_i , corresponding standard deviations $\sigma(R_i)$ and maximum observable changes ΔR_i . Additional data on the open loop voltage V_0 and the heat flow Q , which was measured at the cold side under open loop conditions, are given in S5 within the supplementary information of this article.

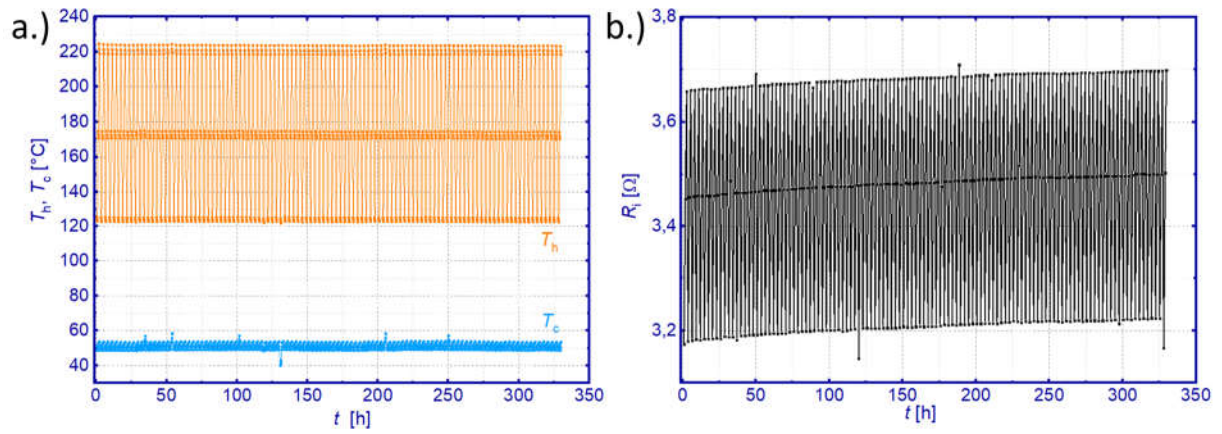


Figure 11: Temperature history (a) and evolution of the temperature dependent electric resistance R_i (b) of module type A in the course of measurements M10.

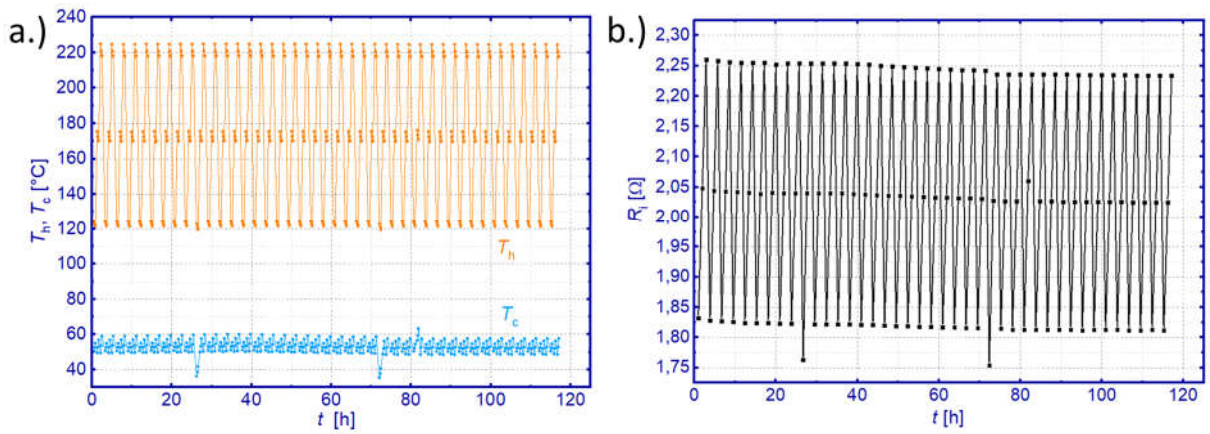


Figure 12: Temperature history (a) and evolution of the temperature dependent electric resistance R_i (b) of module type B in the course of measurements M10.

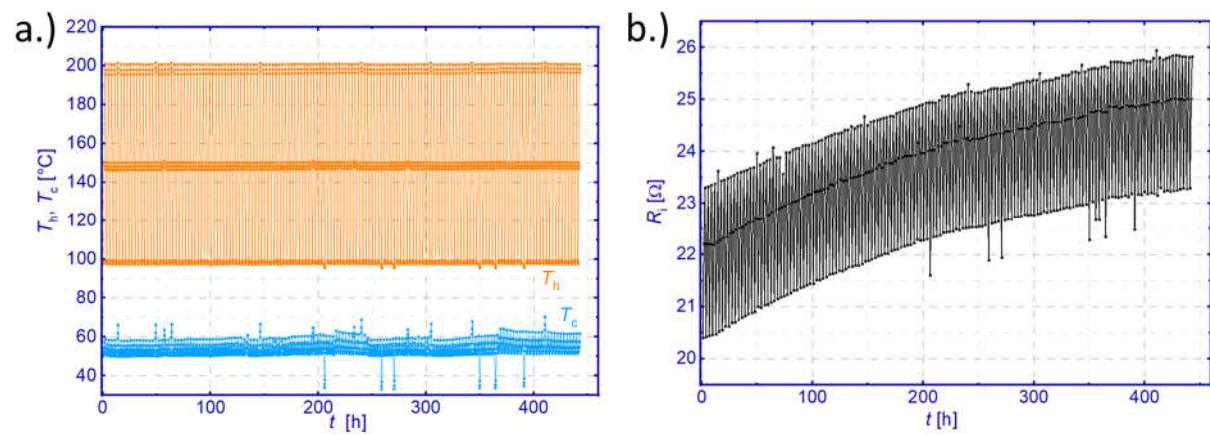


Figure 13: Temperature history (a) and evolution of the temperature dependent electric resistance R_i (b) of module type C in the course of measurements M10.

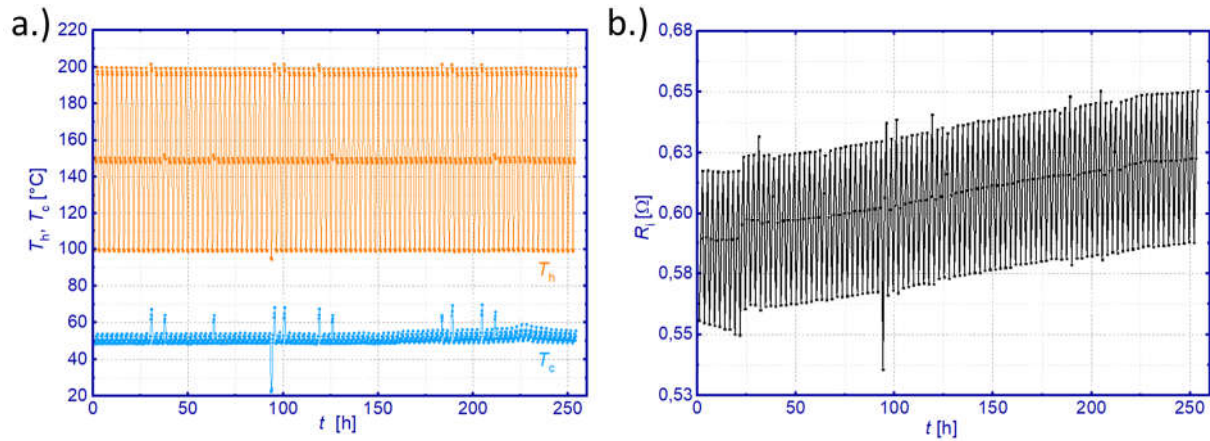


Figure 14: Temperature history (a) and evolution of the temperature dependent electric resistance R_i (b) of module type D in the course of measurements M10.

Table 7 shows a summary of the evaluation of the long-term stability test. The displayed standard deviations have been averaged from temperature dependent data, which is given in Tables S4.

Table 7: The absolute and relative standard deviation $\overline{\sigma(R_i)}$ was averaged from temperature dependent values (Tables S4), which were obtained from results of R_i during M10. The maximum change ΔR_i reflects the maximum observable difference of R_i at any temperature T_H . The relative value of ΔR_i gives the maximum change in relation to the mean value of R_i .

Module type	A	B	C	D
$\overline{\sigma(R_i)}$ [mΩ]	12.67	10.24	803	10.36
$\overline{\sigma(R_i)}$ [%]	0.37	0.52	3.4	1.71
max. ΔR_i [mΩ]	78	78	2900	52.3
max. ΔR_i [%]	2.43	4.3	13.1	9.16

The type A module (Figure 11) showed a minor increase of R_i in the course of M10. The mean standard deviation over the entire temperature range was 12.67 mΩ or 0.37% of the mean value of R_i (Table 7), respectively. This is again below the uncertainty limit of the resistance measurement. The maximum observable change during the entire duration of M10 with 119 thermal cycles for this module type was $\Delta R_i = 78$ mΩ. This equals a maximum ΔR_i per cycle of only 0.65 mΩ. The type B module (Figure 12) confirmed its high stability in the course of M10, too. This module showed a slight trend of decreasing values of R_i . The average standard deviation over the entire temperature range was 10.24 mΩ or 0.52% of the mean value of R_i (Table 7), effectively staying within the measurement uncertainty budget. The maximum observable change was $\Delta R_i = 78$ mΩ. This corresponds to a maximum ΔR_i per cycle of 1.9 mΩ. Both modules showed a stable thermal coupling over the entire duration of M10, as can be seen from the almost constant values of V_0 and Q within the supplementary information S5 (Figures S5-1 and S5-2).

The highest degradation during M10 was observed for module type C (Figure 13) with a monotonous increase of R_i , which showed first signs of stabilization only after 400 h of testing. The mean standard deviation over the entire temperature range was 803 m Ω or 3.4% of the mean value of R_i (Table 7), which is significantly above the measurement uncertainty. The type C module showed the highest absolute and relative change ΔR_i with 2900 m Ω or 13.1%, respectively. Considering the total number of thermal cycles, this corresponds to a maximum ΔR_i per cycle of 19,2 m Ω . Apart from the continuous degradation with regard to R_i , the thermal coupling of the type C module did not remain stable, too. The type C module was the only module showing this behaviour. The unstable thermal coupling can be deduced from data on V_0 and Q within the supplementary information (Figure S5-3), which shows a continuous decrease of V_0 and Q at highest temperature.

Module type D revealed a mean standard deviation over the entire temperature range of 10.36 m Ω or 1.71% of the mean value of R_i (Table 7), which was within the measurement uncertainty budget. However, the maximum change exceeded the uncertainty limit with a value of $\Delta R_i = 52.3$ m Ω corresponding to a maximum relative change of $\Delta R_i = 9.16\%$. This equals a maximum change per temperature cycle of 0.53 m Ω . The type D module showed no irregularities with regard to its thermal coupling, which can be seen by the constant course of V_0 and Q within the supplementary information (Figure S5-4). Nevertheless, this module revealed an abrupt change of the evolution of R_i after approximately 25 h measurement time during M10 (Figure 14), which was not observed during preceding measurement. Initially R_i reduced at lowest T_H and remained almost stable at medium and high temperatures during M10, whereas a monotonous increase has been observed after 25 h.

3.4 Homogeneity (M11)

After M01-M10, further tests were carried out with modules of type A and B only due to their superior stability. In a last step the sample-to-sample scatter (homogeneity) was assessed by the standard deviation of the internal electric resistance $\sigma(R_i)$, which was evaluated with measurement data from M05 and results from three additional modules of type A and B, each. During M11 R_i was measured at a constant cold side temperature of 50 °C and evaluated at discrete hot side temperatures of 100 °C, 150 °C and 200 °C (Table 8).

Table 8: Relative standard deviation of the internal electric resistance $\sigma(R_i)$ among four modules of type A and B, each. The standard deviation is given at three different hot side temperatures in relation to the respective mean values.

$\sigma(R_i)$ [%]	Module type A	Module type B
@ $T_H = 100$ °C	1.21	2.33
@ $T_H = 150$ °C	1.67	3.15
@ $T_H = 200$ °C	3.11	4.15

4. CONCLUSIONS

Commercial Bi₂Te₃-based TEM from four industrial manufacturers were investigated with regard to their stability, similarity and sensitivity of functional properties against variations of the axial pressure. The reported work aimed for the qualification of suitable comparative samples and served as a necessary preparation for a subsequent inter-laboratory comparison of TEM measurements. The module quality was assessed in this work on the base of measurements of the internal electric resistance R_i under various boundary conditions. The uncertainty budget for measurements of R_i was analytically derived and evaluated for every module type. The combined uncertainty was in the range between $1.52\% < u(R_i) < 2.28\%$ and determined from statistic result distributions and quantified sensitivity coefficients for all influencing parameters.

The pressure impact on R_i remained within the measurement uncertainty for modules of type A and B but showed a smooth and expectable course towards slightly lower values of R_i with increasing pressure. Modules of type C and D revealed a higher change of R_i over the entire pressure interval from 2 MPa to 3.5 MPa, effectively exceeding the measurement uncertainty and giving initial indications for a causal pressure influence on R_i . Clear differences could be observed with regard to the module stability, which was investigated in the course of cyclic hot side temperature test with short and long durations of max. 60 h and 443 h, respectively. Absolute changes of R_i yielded standard deviations for type A and B modules, which remained in the double-digit range of mΩ, effectively staying within the measurement uncertainty budgets with few exceptions for the type B module. Long-time stability tests revealed a maximum change of $\Delta R_i = 2.43\%$ and $\Delta R_i = 4.3\%$ for the type A and B module, respectively. A distinctly worse stability was observed for modules of type C and D with maximum changes of $\Delta R_i = 13.1\%$ and $\Delta R_i = 9.16\%$, respectively. The similarity (homogeneity) of R_i was determined in a last step on three additional modules of type A and B only. These tests gave evidence of a measurable lower specimen scatter of type A modules, which was in the range between 1.2% to 3.1% in dependence of the hot side temperature.

Overall, distinct variations could be observed among the tested commercial Bi₂Te₃-based TEMs, which are linked not only to deviating absolute operation parameters but likewise to fundamental differences concerning their functional stability. A detailed cause analysis of observed changes of R_i was not in the focus on this work and would need further measurements and accompanying metallographic investigations. However, the present study supports the assumption of significant quality differences among existent TEM products, which are based on actually mature Bi₂Te₃ technology. According to the results of this study, modules of type A and B revealed not only the highest efficiencies but showed clear advantages concerning their stability. Due to slight benefits with regard to stability and homogeneity modules of type A have been chosen as comparative test samples for a round robin campaign among renowned thermoelectric laboratories, which will be reported in a subsequent publication.

6. ACKNOWLEDGEMENTS

Financial support is gratefully acknowledged for the project “Thermoelectric Standardization for High Temperatures” (TEST-HT, grant number 03VP04401), which was granted by the German Federal Ministry of Education and Research.

7. REFERENCES

- [1] Ebling, D.G; Krumm, A.; Pfeiffelmann, B.; Gottschald, J.; Bruchmann, J.; Benim, A.C.; Adam, M.; Labs, R.; Herbertz, R.R. Development of a System for Thermoelectric Heat Recovery from Stationary Industrial Processes. *Journal of Elec. Materi.* **2016**, Vol. 45:3433, DOI:10.1007/s11664-016-4511-8
- [2] Wang, C.; Tang, S.; Liu, X.; Su, G.H.; Tian, W.; Qiu, S. Experimental study on heat pipe thermoelectric generator for industrial high temperature waste heat recovery, *Applied Thermal Engineering* **2020**, Vo. 175:115299, <https://doi.org/10.1016/j.applthermaleng.2020.115299>.
- [3] Champier, D. Thermoelectric generators: A review of applications, *Energy Conversion and Management* **2017**, Vol 140:167, <https://doi.org/10.1016/j.enconman.2017.02.070>.
- [4] Rodriguez, R.; Preindl, M., Cotton; J. S., Emadi, A. Review and Trends of Thermoelectric Generator Heat Recovery in Automotive Applications, *IEEE Transactions on Vehicular Technology* 2019, Vol. 68:5366, DOI: 10.1109/TVT.2019.2908150
- [5] Heghmanns, A.; Wilbrecht, S.; Beitel Schmidt, M.; Geradts, K. Parameter Optimization and Operating Strategy of a TEG System for Railway Vehicles, *Journal of Elec. Materi.* **2016**, Vol. 45:1633, DOI: 10.1016/j.matpr.2015.05.098
- [6] Kristiansen, N.R.; Snyder, G.J.; Nielsen, H.K.; Rosendahl, L. Waste Heat Recovery from a Marine Waste Incinerator Using a Thermoelectric Generator, *Journal of Elec. Materi.* **2012**, Vol. 41:1024, DOI: 10.1007/s11664-012-2009-6
- [7] Singh, D.V.; Pedersen, E. A review of waste heat recovery technologies for maritime applications, *Energy Conversion and Management* **2016**, Vol. 111:315, <https://doi.org/10.1016/j.enconman.2015.12.073>
- [8] D. M. Rowe, "Chapter 1. General Principles and Basic Considerations " in Rowe, D. M.(ed.), *Thermoelectric Handbook - Macro to Nano*, Boca Raton, USA: Taylor & Francis Group, 2006, p. 1–1. doi:10.1201/9781420038903.sec1
- [9] Ioffe, A. F.; Stilbans, L. S.; Iordanishvili, E. K.; Stavitskaya, T. S.; Gelbtuch, A.; Vineyard, G. Semiconductor Thermoelements and Thermoelectric Cooling. *Physics Today* **1959**, 12:42.
- [10] Salvador, J.R.; Cho, J.Y.; Ye, Z.; Moczygemba, J.E.; Thompson, A.J.; Sharp, J.W.; König, J.D.; Maloney, R.; Thompson, T.; Sakamoto, J.; Wang, H.; Wereszczak, A.A.; Meisner, G.P. Thermal to Electrical Energy Conversion of Skutterudite-Based Thermoelectric Modules. *J. of Elec Materi* **2013**, Vol. 42:1389, <https://doi.org/10.1007/s11664-012-2261-9>
- [11] Ochi, T.; Nie, G.; Suzuki, S.; Kikuchi, M.; Ito, S.; Guo, J.Q. Power-Generation Performance and Durability of a Skutterudite Thermoelectric Generator. *Journal of Elec. Materi.* **2014**, Vol. 43:2344, doi:10.1007/s11664-014-3060-2
- [12] Garcia-Canadas, J.; Powell, A.V.; Kaltzoglou, A.; Vaqueiro, P.; Min, G. Fabrication and Evaluation of a Skutterudite-Based Thermoelectric Module for High-Temperature Applications. *Journal of Elec Materi* **2013**, Vol. 42:1369, <https://doi.org/10.1007/s11664-012-2241-0>
- [13] Bartolomé, K.; Balke, B.; Zuckermann, D.; Köhne, M.; Müller, M.; Tarantik, K.; König, J. Thermoelectric Modules Based on Half-Heusler Materials Produced in Large Quantities. *Journal of Elec Materi* **2014**, Vol. 43:1775, <https://doi.org/10.1007/s11664-013-2863-x>
- [14] TEC TEG MFR. - <https://thermoelectric-generator.com/teg-cascade-800c-hot-side-thermoelectric-power-modules> (accessed: October 9, 2020)
- [15] Novus Energy Technologies - http://www.novusenergytechnologies.com/technologies/power_generation.html (accessed: October 9, 2020)
- [16] Kryotherm - <http://kryothermtec.com/medium-temperature-generating-modules-mars-series.html> (accessed: October 9, 2020)
- [17] Joshi, G.; Poudel, B. Efficient and Robust Thermoelectric Power Generation Device Using Hot-Pressed Metal Contacts on Nanostructured Half-Heusler Alloys. *Journal of Elec Materi* **2016**, Vol. 45:6047, doi:10.1007/s11664-016-4692-1

-
- [18] Zhang, Q.; Liao, J.; Tang, Y.; Gu, M.; Ming, C.; Qiu, P.; Bai, S.; Uher, C.; Chen, L. Realizing a thermoelectric conversion efficiency of 12% in bismuth telluride/skutterudite segmented modules through full-parameter optimization and energy-loss minimized integration. *Energy Environ. Sci.* **2017**, Vol. 10:956, doi:10.1039/C7EE00447H
- [19] Chetty, R.; Nagase, K.; Aihara, M.; Jood, P.; Takazawa, H.; Ohta, M.; Yamamoto, A. Mechanically durable thermoelectric power generation module made of Ni-based alloy as a reference for reliable testing. *Applied Energy* **2020**, 114443, <https://doi.org/10.1016/j.apenergy.2019.114443>.
- [20] Ziolkowski, P.; Chetty, R.; Blaschkewitz, P.; Ohta, M.; Yamamoto, A.; Müller, E. Inter-Laboratory Testing for High Temperature Power Generation Characteristics of a Ni-Based Alloy Thermoelectric Module. *Energy Technology* **2020**, Vol. ??:??, DOI: 10.1002/ente.202000557
- [21] Kajikawa, T. Overview of Thermoelectric Power Generation Technologies in Japan, in Thermoelectrics application meeting of the U.S. Office of Energy Efficiency and Renewable Energy, http://www1.eere.energy.gov/vehiclesandfuels/pdfs/thermoelectrics_app_2011/tuesday/kajikawa.pdf (accessed: May 15, 2020).
- [22] Hi-Z- <https://hi-z.com/products/> (accessed: October 9, 2020).
- [23] II-VI Marlow - <https://www.marlow.com/products/power-generators/thermoelectric-generator-teg-modules> (accessed: October 9, 2020).
- [24] Kryotherm - <http://kryothermtec.com/thermoelectric-modules-for-power-generation.html> (accessed: October 9, 2020).
- [25] Komatsu - <https://www.kelk.co.jp/english/products/generation.html> (accessed: October 9, 2020).
- [26] Evonik - <https://www.espryx.com/product/thermoelectric-generators/en/> (accessed: October 9, 2020).
- [27] Thermanamic - <http://www.thermonamic.com/products.asp?cid=384> (accessed: October 9, 2020).
- [28] Hachiuma, H. Activities and Future Vision of Komatsu Thermo modules, in: 5th European Conference on Thermoelectrics, 2007, Odessa, Ukraine. URL: <http://ect2007.its.org/ect2007.its.org/system/files/u1/pdf/01.pdf> (accessed: October 9, 2020).
- [29] Brostow, W.; Datashvili, T.; Hagg Lobland, H.E.; Hilbig, T.; Su, L.; Vinado, C., White, J. Bismuth telluride-based thermoelectric materials: Coatings as protection against thermal cycling effects. *Journal of Materials Research* **2012**, Vol 27, 22, pp. 2930-2936.
- [30] Zheng, Y.; Tan, X.J.; Wan, X.; Cheng, X.; Liu, Z.; Yan, Q. Thermal Stability and Mechanical Response of Bi₂Te₃-Based Materials for Thermoelectric Applications, *ACS Appl. Energy Mater.* **2020**, 3, pp. 2078–2089. <https://doi.org/10.1021/acsaem.9b02093>
- [31] Lee, D.M.; Lim, C.H.; Cho, D.C.; Lee, Y. S.; Lee, C. H. Effects of annealing on the thermoelectric and microstructural properties of deformed n-type Bi₂Te₃-based compounds. *Journal of Electronic Materials* **2006**, Vol. 35:360. <https://doi.org/10.1007/BF02692457>
- [32] Zhao, L.D.; Zhang, B.-P.; Liu, W.S.; Zhang, H.L.; Li, J.-F. Effects of annealing on electrical properties of n-type Bi₂Te₃ fabricated by mechanical alloying and spark plasma sintering. *Journal of Alloys and Compounds* **2009**, Vol. 467, pp. 91-97. <https://doi.org/10.1016/j.jallcom.2007.12.063>.
- [33] Yamashita, O.; Tomiyoshi, S. High performance n-type bismuth telluride with highly stable thermoelectric figure of merit. *Journal of Applied Physics* **2004**, Vol. 95:6277. <https://doi.org/10.1063/1.1712013>
- [34] Chen, S.; Cai, K.F.; Li, F.Y.; Shirley, S.Z. The Effect of Cu Addition on the System Stability and Thermoelectric Properties of Bi₂Te₃. *Journal of Electronic Materials* **2013**, Vol. 43, pp. 1966-1971. DOI: 10.1007/s11664-013-2928-x.
- [35] Lognoné, Q.; Gascoin, F. Reactivity, stability and thermoelectric properties of n-Bi₂Te₃ doped with different copper amounts. *Journal of Alloys and Compounds* **2014**, Vol. 610, pp. 1-5. <https://doi.org/10.1016/j.jallcom.2014.04.166>.

-
- [36] He, W.; Zhang, G.; Zhang, X.; Ji, J.; Li, G.; Zhao, X. Recent development and application of thermoelectric generator and cooler. *Applied Energy* **2015**, Vol. 143, pp. 1-25. <https://doi.org/10.1016/j.apenergy.2014.12.075>.
- [37] Chen, Y.; Hou, X.; Ma, C.; Dou, Y.; Wu, W. Review of Development Status of Bi₂Te₃-Based Semiconductor Thermoelectric Power Generation. *Advances in Materials Science and Engineering* **2018**, Vol. 2018:1210562. <https://doi.org/10.1155/2018/1210562>
- [38] ISO/REMCO Committee on reference materials, ISO Guide 35:2017 Reference Materials—Guidance for characterization and assessment of homogeneity and stability (ISO, 2017)., (n.d.). <https://www.iso.org/standard/60281.html> (accessed: October 9, 2020).
- [39] Ziolkowski, P.; Stiewe, C.; de Boor, J.; Druschke, I.; Zabrocki, K.; Edler, F.; Haupt, S.; König, J.; Müller, E. Iron Disilicide as High-Temperature Reference Material for Traceable Measurements of Seebeck Coefficient Between 300 K and 800 K. *Journal of Electronic Materials* **2017**, Vol.46:51, <https://doi.org/10.1007/s11664-016-4850-5>
- [40] Lowhorn, N.; Wong-Ng, W.; Lu, Z.; Martin, J.; Green, M.; Bonevich, J.; Thomas, E.; Dilley, N.; Sharp, J. Development of a Seebeck coefficient Standard Reference Material. *Journal of Materials Research* 2011, Vol.26:1983, doi:10.1557/jmr.2011.118
- [41] Borup, K.A.; de Boor, J.; Wang, H.; Drymiotis, F.; Gascoin, F.; Shi, X.; Chen, L.; Fedorov, M.I.; Müller, E.; Iversen, B.B.; Snyder, G.J. Measuring thermoelectric transport properties of materials, *Energy Environ. Sci.* **2015**, Vol.8:423, <https://doi.org/10.1039/C4EE01320D>
- [42] Martin, J.; Tritt, T.; Uher, C. High temperature Seebeck coefficient metrology, *Journal of Applied Physics* **2010**, Vol.108:121101, <https://doi.org/10.1063/1.3503505>
- [43] Wang, H.; Porter, W.D.; Böttner, H.; König, J.; Chen, L.; Bai, S.; Tritt, T.M.; Mayolet, A.; Senawiratne, J.; Smith, C.; Harris, F.; Gilbert, P.; Sharp, J.W.; Lo, J.; Kleinke, H.; Kiss, L. Transport Properties of Bulk Thermoelectrics - An International Round-Robin Study, Part I: Seebeck Coefficient and Electrical Resistivity, *J. Electron. Mater.* **2013**, vol. 42:654, <https://doi.org/10.1007/s11664-012-2396-8>
- [44] Wang, H.; Bai, S.; Chen, L.; Cuenat, A.; Joshi, G.; Kleinke, H.; König, J.; Lee, H.W.; Martin, J.; Oh, M.-W.; Porter, W.D.; Ren, Z.; Salvador, J.; Sharp, J.; Thompson, P.T.A.J.; Tseng, Y.C. International Round-Robin Study of the Thermoelectric Transport Properties of an *n*-Type Half-Heusler Compound from 300 K to 773 K, *J. Electron. Mater.* 2015, Vol:44:4482, <https://doi.org/10.1007/s11664-015-4006-z>
- [45] Lowhorn, N.D.; Wong-Ng, W.; Zhang, W.; Lu, Z.Q.; Otani, M.; Thomas, E.; Green, M.; Tran, T.N.; Dilley, N.; Ghamaty, S.; Elsner, N.; Hogan, T.; Downey, A.D.; Jie, Q.; Li, Q.; Obara, H.; Sharp, J.; Caylor, C.; Venkatasubramanian, R.; Willigan, R.; Yang, J.; Martin, J.; Nolas, G.; Edwards, B.; Tritt, T. Round-robin measurements of two candidate materials for a Seebeck coefficient Standard Reference Material. *App. Phys. A* **2009**, Vol. 94:231, doi:10.1007/s00339-008-4876-5.
- [46] Ziolkowski, P.; Blaschkewitz, P.; Müller, E. Heat Flow Measurement as a key to Standardization of Thermoelectric Generator Module Metrology: A Comparison of reference and absolute Techniques, *Measurement* **2021**, Vol. 167:108273, <https://doi.org/10.1016/j.measurement.2020.108273>.
- [47] Isabellenhütte PBV product brochure https://www.isabellenhuetten.de/fileadmin/Daten/Praezisionswiderstaende/IHH_Bauelementebroschuere_dt.pdf (accessed: October 6, 2020).
- [48] CalPlus, Keithley 2700 manual, <https://www.calplus.de/fileuploader/download/download/?d=0&file=custom%2Fupload%2Fkeithley-2700-handbuch-feb-2016.pdf> (accessed: October 6, 2020)
- [49] Liao, M.; He, Z.; Jiang, C.; Fan, X.; Li, Y.; Qi, F. A three-dimensional model for thermoelectric generator and the influence of Peltier effect on the performance and heat transfer. *Applied Thermal Engineering* **2018**, Vol. 133:493, <https://doi.org/10.1016/j.applthermaleng.2018.01.080>
- [50] BIPM, IEC, IFCC, ILAC, ISO, IUPAC, IUPAP, OIML. Guide to the Expression of Uncertainties in Measurement. Joint Committee for Guides in Metrology 100:2008, GUM 1995 with minor

-
- corrections, <http://www.bipm.org/utis/common/documents/jcgm/JCGM 100 2008 E.pdf> (accessed: October 6, 2020)
- [51] Hässelbarth, W., *BAM-Leitfaden zur Ermittlung von Messunsicherheiten bei quantitativen Prüfergebnissen - 1. Fassung März 2004*. 2004, Wirtschaftsverlag NW: Bremerhaven. p. 1-52. <http://d-nb.info/991763459> (accessed: October 7, 2020).
- [52] Araiz, M.; Catalan, L.; Herrero, O.; Perez, G.; Rodriguez, A. The importance of the assembly in thermoelectric generators. In *Bringing Thermoelectricity into Reality*; Aranguren, P., Ed.; IntechOpen: London, UK, **2018**; pp. 123–144; ISBN 978-1-78923-440-4
- [53] Salvador, J.R.; Cho, J.Y.; Ye, Z.; Moczygemba, J.E.; Thompson, A.J.; Sharp, J. W.; Koenig, J.D.; Maloney, R.; Thompson, T.; Sakamoto, J.; Wang, H.; Wereszczak, A.A. Conversion efficiency of skutterudite-based thermoelectric modules. *Phys. Chem. Chem. Phys.* **2014**, Vol. 16:12510. DOI: 10.1039/C4CP01582G
- [54] Karthick, K.; Joy, G.C.; Suresh, S.; Dhanuskodi, R. Impact of Thermal Interface Materials for Thermoelectric Generator Systems. *Journal of Elec Materi* **2018**, Vol. 47:5763. <https://doi.org/10.1007/s11664-018-6496-y>
- [55] Saviers, K.R.; Hodson, S.L.; Fisher, T.S.; Salvador, J.R.; Kasten, L.S. Carbon Nanotube Arrays for Enhanced Thermal Interfaces to Thermoelectric Modules. *Journal of Thermophysics and Heat Transfer* **2013**, Vol. 27:3. <https://doi.org/10.2514/1.T4026>
- [56] Wang, S.; Xie, T.; Xie, H. Experimental study of the effects of the thermal contact resistance on the performance of thermoelectric generator. *Applied Thermal Engineering* **2018**, Vol. 130:847. <https://doi.org/10.1016/j.applthermaleng.2017.11.036>
- [57] Karthick, K.; Suresh, S.; Singh, H.; Joy, G.C.; Dhanuskodi, R. Theoretical and experimental evaluation of thermal interface materials and other influencing parameters for thermoelectric generator system, *Renewable Energy* **2019**, Vol. 134:25. <https://doi.org/10.1016/j.renene.2018.10.109>
- [58] Hatzikraniotis, E.; Zorbas, K.T.; Samaras, I.; Kyratsi, Th.; Paraskevopoulos, K.M. Efficiency Study of a Commercial Thermoelectric Power Generator (TEG) Under Thermal Cycling. *Journal of Electronic Materials* **2010**, Vol.39:9. DOI: 10.1007/s11664-009-0988-8
- [59] Barako, M.T.; Park, W.; Marconnet, A.M.; Asheghi, M.; Goodson, K.E. Thermal Cycling, Mechanical Degradation, and the Effective Figure of Merit of a Thermoelectric Module. *Journal of Electronic Materials* **2013**, Vol 42:3. DOI: 10.1007/s11664-012-2366-1
- [60] Ochi, T.; Nie, G.; Suzuki, S.; Kikuchi, M.; Ito, S.; Guo, J.Q. Power-Generation Performance and Durability of a Skutterudite Thermoelectric Generator. *Journal of Electronic Materials* **2014**, Vol. 43:6. DOI: 10.1007/s11664-014-3060-2
- [61] Broz, P.; Zelenka, F.; Kohoutek, Z.; Vrestal, J.; Vykoukal, V.; Bursik, J.; Zemanova, A.; Rogl, G.; Rogl, P. Study of thermal stability of CoSb₃ skutterudite by Knudsen effusion mass spectrometry, *Calphad* **2019**, Vol. 65:1. <https://doi.org/10.1016/j.calphad.2019.01.012>
- [62] Battiston, S.; Montagner, F.; Fiameni, S.; Famengo, A.; Boldrini, S.; Ferrario, A.; Fanciulli, C.; Agresti, F.; Fabrizio, M. AlTiN based thin films for degradation protection of tetrahedrite thermoelectric material. *Journal of Alloys and Compounds* **2019**, Vol. 792:953. <https://doi.org/10.1016/j.jallcom.2019.04.116>
- [63] Tenório, H.; Vieira, D.A.; Souza, C.P. Measurement of parameters and degradation of thermoelectric modules. *IEEE Instrumentation and Measurement Magazine* **2017**, Vol.20(2):13-19. DOI: 10.1109/MIM.2017.7919127
- [64] Jood, P.; Ohta, M. Temperature-Dependent Structural Variation and Cu Substitution in Thermoelectric Silver Selenide. *ACS Appl. Energy Mater.* **2020**, 3, 3, 2160–2167. <https://doi.org/10.1021/acsaem.9b02231>.
- [65] Wang, L.; Lu, X.; Yu, X.; Wang, Q.; Zhao, D.; Ren, W.; Ma, T. Effect of Operating Temperature on Interface Diffusion and Power Generation of Bismuth Telluride Thermoelectric Modules. *Heat Transfer Research* **2020**, Vol. 51:3. DOI: 10.1615/HeatTransRes.2019030539
- [66] Padoue Shyikira, A.; Skomedal, G.; Middleton, P.H. Performance evaluation and stability of silicide-based thermoelectric modules. *Materials Today: Proceedings* **2020**, in press, <https://doi.org/10.1016/j.matpr.2020.05.193>.

-
- [67] Chen, L.-W.; Wang, C.; Liao, Y.-C.; Li, C.-L.; Chuang, T.-H.; Hsueh, C.-H. Design of diffusion barrier and buffer layers for β -Zn₄Sb₃ mid-temperature thermoelectric modules. *Journal of Alloys and Compounds* **2018**, Vol. 762:631. <https://doi.org/10.1016/j.jallcom.2018.05.251>.